Measurement of Antenna Patterns for Oceanographic Radars Using Aerial Drones

LIBE WASHBURN

Marine Science Institute, and Department of Geography, University of California, Santa Barbara, Santa Barbara, California

EDUARDO ROMERO AND CYRIL JOHNSON

Marine Science Institute, University of California, Santa Barbara, Santa Barbara, California

BRIAN EMERY

Marine Science Institute, and Department of Mechanical Engineering, University of California, Santa Barbara, Santa Barbara, California

CHRIS GOTSCHALK

Marine Science Institute, University of California, Santa Barbara, Santa Barbara, California

(Manuscript received 16 September 2016, in final form 28 February 2017)

ABSTRACT

A new method is described employing small drone aircraft for antenna pattern measurements (APMs) of high-frequency (HF) oceanographic radars used for observing ocean surface currents. Previous studies have shown that accurate surface current measurements using HF radar require APMs. The APMs provide directional calibration of the receive antennas for direction-finding radars. In the absence of APMs, so-called ideal antenna patterns are assumed and these can differ substantially from measured patterns. Typically, APMs are obtained using small research vessels carrying radio signal sources or transponders in circular arcs around individual radar sites. This procedure is expensive because it requires seagoing technicians, a vessel, and other equipment necessary to support small-boat operations. Furthermore, adverse sea conditions and obstacles in the water can limit the ability of small vessels to conduct APMs. In contrast, it is shown that drone aircraft can successfully conduct APMs at much lower cost and in a broader range of sea states with comparable accuracy. Drone-based patterns can extend farther shoreward, since they are not affected by the surfzone, and thereby expand the range of bearings over which APMs are determined. This simplified process for obtaining APMs can lead to more frequent calibrations and improved surface current measurements.

1. Introduction

High-frequency (HF) radar is currently one of the few technologies capable of measuring surface currents over broad areas of the coastal ocean. Depending on the transmit frequency and processing procedures, these radars are capable of measuring time series of current vectors at subhourly sampling intervals and on scales of about 250 m and larger. An individual radar measures the radial components of surface current velocities (radials) directed either toward or away from the radar. The offshore coverage range for obtaining radials from individual radars extends from about 20 km for 42-MHz systems to about 200 km for 5-MHz systems.

HF radars for ocean surface current measurement are a backbone technology of evolving coastal ocean observing systems worldwide. For example, during 2016 the U.S. Integrated Ocean Observing System (IOOS) operated an array of ~135 HF radars with coverage spanning much of the coastline of the United States, including Hawaii and Alaska. About 85% of these radars are SeaSondes (manufactured by CODAR Ocean Sensors, Ltd.) and use direction-finding (DF) techniques to determine arrival directions of radials on the sea surface. The remaining systems have linear phased array antennas and can use

Corresponding author e-mail: Libe Washburn, libe.washburn@ucsb.edu

DOI: 10.1175/JTECH-D-16-0180.1

either DF or beamforming (BF) techniques to determine arrival directions of radials.

A critical function of HF radars is the ability to identify the directions of arrival of signals backscattered from the sea surface. These signals result from Bragg scattering of transmitted radio waves by ocean surface gravity waves with wavelengths λ_B equaling half the transmitted wavelength λ (e.g., for 14-MHz radars, $\lambda_B = \lambda/2 = 21.4\,\text{m}/2 = 10.7\,\text{m}$). Signal processing methods used by DF radars divide the coverage area offshore of individual radars into a series of circular range cells of widths of 1–6 km depending on transmit frequency bandwidth. Each range cell is divided into azimuthal sectors spanning angles of typically 1°–5° by the direction-finding procedure. Radials are estimated simultaneously over each range cell within coverage. Within a range cell, radials are separated according to their Doppler frequencies using fast Fourier transforms (FFTs). Given the transmit frequency f and the sweep rate f_s of a radar, the Doppler resolution of radial speed Δv_r depends on the integration time Mf_s^{-1}, where M is the FFT length. As an example, for $f = 14\,\text{MHz}$ and $f_s = 2\,\text{Hz}$, typical of radars in this study, with $M = 512$, $\Delta v_r = c/(2Mf_s^{-1}f) = 0.042\,\text{m s}^{-1}$, where c is the speed of light ($3.00 \times 10^8\,\text{m s}^{-1}$). Longer FFTs produce smaller Δv_r at the cost of reduced temporal resolution.

Placing the radials at bearings within a range cell depends on determining the direction of arrival (DOA) corresponding to each radial velocity (Lipa and Barrick 1983; de Paolo and Terrill 2007). Determining the DOA relies on algorithms such as multiple signal classification (MUSIC; Schmidt 1986). A key factor for determining DOAs with the MUSIC algorithm is knowing the directional response of the receive antenna array. For DF radars, including SeaSondes, the directional response is determined through direct measurement. In practice the antenna pattern measurements (APMs) take the form of tables specifying the responses of the three receive antenna elements at each bearing. Similar procedures can be performed for phased array radars (Fernandez et al. 2003; Flores-Vidal et al. 2013).

Measurement of APMs is critical for accurate estimates of radials and the total current vectors computed from the radials (Barrick and Lipa 1999; Kohut and Glenn 2003; Paduan et al. 2006; Cosoli et al. 2010; Flores-Vidal et al. 2013). In the absence of APMs, so-called ideal patterns are used in the MUSIC algorithm. For SeaSondes these are based on the theoretical sinusoidal directional responses of the loop antenna elements (Lipa and Barrick 1983). For phased array radars, these are equivalent to assuming known phase offsets due to physical separation of receive elements and uniform amplitude patterns for all elements over all bearings. Ideal patterns can differ substantially from measured patterns, resulting in systematic errors in the radials and total surface current vectors.

One method for obtaining APMs is to conduct field operations in which a small research vessel carries a radio signal source, such as a transponder, in circular arcs around individual radar sites. This method is expensive, since it requires the use of a vessel and skilled personnel. It can also be problematic due to adverse winds and sea states and the remoteness of many HF radar sites from launch points for small vessels. Alternate methods for APMs employ ships of opportunity with unknown positions (Flores-Vidal et al. 2013; Fernandez et al. 2006) or known positions based on Automatic Identification System transmitters (Emery et al. 2014).

Here we describe a new approach to APMs using small autonomous aerial vehicles (drones) carrying miniature radio frequency signal sources. Section 2 describes the two types of drones that we have used for APMs along with the radio signal sources they carried. We also estimated the accuracy of determining horizontal position from GPS fixes and vertical position from barometric pressure measurements. Section 3 illustrates APMs obtained using the drones and compares them with the conventional vessel-based approach. We also compare the abilities of the drones and boats to follow accurately circular arcs during APMs. Section 4 summarizes our use of drones for APMs and suggests future directions.

2. Methods

Newly available low-cost drone technologies have allowed our laboratory to pursue their use for APMs. Five recent developments have enabled drone-based APMs: 1) low-cost microprocessor-based control technologies for robotic control of small aircraft (e.g., Kissack 2012); 2) miniaturized, accurate GPS receivers for maintaining precise flight trajectories; 3) small, lightweight batteries with high energy storage densities for extended flight durations; 4) low-cost three-dimensional (3D) printers for fabricating small, lightweight aircraft components without the need for expensive machining; and 5) the development of a lightweight, self-contained radio signal source that can be carried by drones.

All of our experiments have employed battery-based energy storage rather than combustible fuels. This simplifies field operations and lessens the risk of fire. In our early experiments, we used fixed-wing airplane drones (planes) due to limitations in battery capacity. In later experiments when higher-capacity batteries had become available, we began using quadrotor drones (quadrotors).

We describe the use of both types of drones for APMs, but we now exclusively use quadrotors due to their simpler operating requirements.

a. Airplane drone

Our first experiments for drone-based APMs employed a small plane constructed mainly from lightweight expanded polyolefin foam. In addition to its low density, an advantage of an airplane constructed from foam is that it floats if it lands in water, which aids recovery. The plane used was a Super Sky Surfer manufactured in China and sold on the Internet. The plane was a conventional monoplane design with a vertical stabilizer and elevator. The wingspan was 2.40 m and the fuselage length was 1.35 m. The stated glide ratio of the plane was 16 to 1.

The plane was largely preassembled, although a few changes were made to increase structural strength while reducing weight. For example, the plane was delivered with a solid fiberglass rod, 1.27 cm in diameter and 1.22 m long, mounted inside the wing for rigidity. This was replaced with a thin-walled carbon fiber tube of similar dimensions but less than a third of the weight. The mass of the airplane drone, including battery and radio signal source, was 2.46 kg. A single wheel mounted on the centerline of the fuselage allowed the plane to rollout after landing. The plane was delivered with moveable control surfaces incorporated into the rudder and elevator, and ailerons were placed in the trailing sections of the wings. Control surfaces were moved using small servos. All surfaces could be controlled manually by a human operator using a hobby-level radio-control (RC) transmitter and receiver. For APMs the plane was autonomously controlled.

Automated flight control employed ArduPilot components and software for small drones (e.g., ArduPilot.org). Software included so-called fail-safe techniques, such as return to launch, if radio communications with the plane were lost. An onboard GPS receiver determined position. The flight control hardware and GPS were enclosed in a waterproof plastic bag for protection in the event of a water landing. The flight controller was mounted inside the fuselage in front of the wing, where a model cockpit and model human pilot were placed in the original design. The GPS module containing the antenna was mounted on the top of the plane with the antenna exposed through a small opening cut out of the fuselage. The autopilot's inertial measurement unit logged in-flight data, such as altitude, battery voltage, pitch, yaw, roll, compass heading, airspeed, and GPS position, at 2 Hz. Altitude was measured with a barometer and airspeed was measured with a Pitot tube mounted on the wing.

The plane was powered by an electric motor and a lightweight rechargeable battery. A 12-pole brushless motor turned the airplane's propeller at 6000 revolutions per minute (rpm) to produce the 17 km r^{-1} airspeed used for APMs. The stall speed of the airplane was about 14 km h^{-1}. The two-bladed, 23-cm-diameter plastic propeller was mounted in a pusher configuration on a pylon above the wing. The propeller rotation rate could be changed using RC by a human operator or by the flight controller. An electronic speed controller regulated the propeller rotation rate and powered onboard systems such as the servos for moving the control surfaces. A number of batteries were tried, but the one used most often was a lithium polymer (LiPo) battery with three cells in series that produced 12.6 V. The LiPo battery had 8400-mAh capacity and a mass of 0.62 kg, or about a quarter of the airplane's total mass. This battery gave the plane a flight duration of about 1.5 h

For a typical APM the plane was hand launched, usually from a beach, at a point about 2.5 km from the HF radar site. Following launch, the plane climbed to about 45-m altitude, where it flew in circles to confirm that the autopilot was working properly. The plane then conducted the APMs by flying in two semicircular arcs 2.5 km in radius offshore of the radar site. One arc was performed while traveling away from the launch point and the other while traveling back toward the launch point. Both arcs were flown on a single battery charge. The 2.5-km radius was chosen such that the plane traversed 180° of bearing in about 27 min at its 17.4 km h^{-1} cruising speed. This ensured a dwell time of about 9 s per degree azimuth for the APMs. The airplane flew about 75 m above the sea surface during the APMs.

The onboard flight controller and GPS were able to maneuver the plane to accurately follow circular arcs to within a few meters as shown below. Following the APM, the plane was landed either under autonomous control or under manual RC by a human operator. Flights were conducted in the early morning, when winds were light and few people were on the landing beaches. A typical APM lasted about 45 min from launch to landing. A single technician (author ER) carried out the APMs.

b. Quadrotor drone

As motor efficiency and battery capacity increased, we began experimenting with quadrotors for APMs. Quadrotors and other multirotor drones have three principal advantages over airplane drones for APMs: 1) they can be flown in higher wind; 2) they can take off and land vertically; and 3) they can be flown at slower horizontal speeds, which allows APMs to be conducted closer to shore with smaller flight trajectory arcs. This last point is important, since evolving rules regulating flight operations require drones to be within sight of a human operator without optical aid.

Initially we constructed quadrotors in our laboratory for APMs, but now we exclusively use commercially available quadrotors for APMs. The development of small multirotor drones is rapidly advancing and now commercial quadrotors are available that meet the requirements for use in APMs: 1) capability to fly accurate preprogramed flight trajectories and 2) sufficient battery duration to fly arcs with radii of a few hundred meters around receive antenna arrays while carrying the signal source payload. For example, as of this writing (fall 2016) we use the 3DR Solo Smart Drone (see https://3dr.com/solo-drone/), but given the advancing technology it seems unlikely that this drone will remain available. We expect that an increasing number of commercially available multirotor drones will be capable of APMs. Therefore, we do not focus here on the specific characteristics of any particular multirotor drone.

For APMs, we flew the quadrotors in two circular arcs in opposite directions centered on the receive antenna locations at the radar sites. The purpose of the two arcs was to reduce bias in bearing due to discrepancies between the HF radar site computer clock and the drone clock. After some experimentation we determined that a radius of 300 m produced APMs that matched well the boat and plane APMs as explained below, although the results did not depend strongly on the radius. The altitude during the APMs was about typically 10–20 m above the sea surface, but we also experimented with other altitudes. Flights were conducted in the early morning, when winds were light. Each arc required 15–20 min of flying time. When using the commercial quadrotor, two flights were made and the battery was swapped between arcs. For the quadrotor made in our laboratory, the battery duration (~45 min) was sufficient to complete both arcs during a single flight. Following APMs, the quadrotors landed either under autonomous control or under manual RC by a human operator.

c. *Radio frequency signal source for the planes*

The payloads carried by the drones for APMs were small, lightweight signal sources designed by one of the authors (CJ) and constructed by another author (ER). These could produce 10-mW signals over a range of user-selectable frequencies in the HF band. For the plane, the signal source was powered by a 12.6-V lithium polymer battery, and the electronics package, including the battery, was mounted inside the fuselage. The signal source was connected to a 5.5-m-long monopole antenna made from 18-gauge wire. At this length, the antenna corresponded to about one-quarter wavelength at a transmit frequency of 13.6 MHz. The ground plane for the antenna was constructed from copper tape attached to the underside of the wing. During initial experiments about 20% of the wing area was covered with the copper tape. To save weight, this was later reduced to about 10% of the wing area with no significant loss of transmit efficiency. A radio-controlled hook assembly allowed the monopole antenna to be dropped before landing.

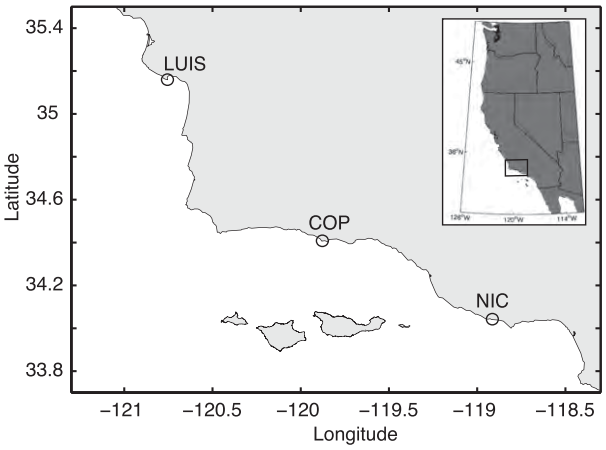

FIG. 1. Study area where antenna pattern measurements described in text were conducted. Circles indicate sites at Nicholas Canyon (NIC), Coal Oil Point (COP), and Port San Luis (LUIS).

An important characteristic of the signal source was its frequency stability. Previous APM methods used a transponder as a signal source (Lipa and Barrick 1983; Barrick and Lipa 1999) that received, modified, and retransmitted the signal originating from the HF radar site. This technique created a transponder signal that was stable in frequency within a few tenths of a hertz.

During APMs conducted with our drone signal source, the transmitter was turned off at the HF radar site. Consequently, there was no synchronization with the receiver, such as with a transponder, so the signal source had to independently produce a frequency-stable signal. To produce such a signal, a voltage-controlled, temperature-compensated crystal oscillator was used. The oscillator specification was ±0.5 ppm at 25°C (±2.5 ppm over −30° to +75°C), allowing it to produce HF frequencies that were stable to within a few tenths of a hertz over the course of the APM. The stability of the signal reduced spreading of the signal between FFT bins in the processing of the antenna patterns. With these characteristics, the signal-to-noise ratio of the received signal was typically near 50 for both the signal sources carried by both drones.

d. *Radio signal source for quadrotors*

The signal source for the quadrotor drone, a smaller version of the source used for the plane, consisted of a smaller electronics board and a similar battery. The source was connected to a center-fed dipole antenna. A dipole design was used because an efficient ground plane, necessary for a monopole antenna, would have been difficult

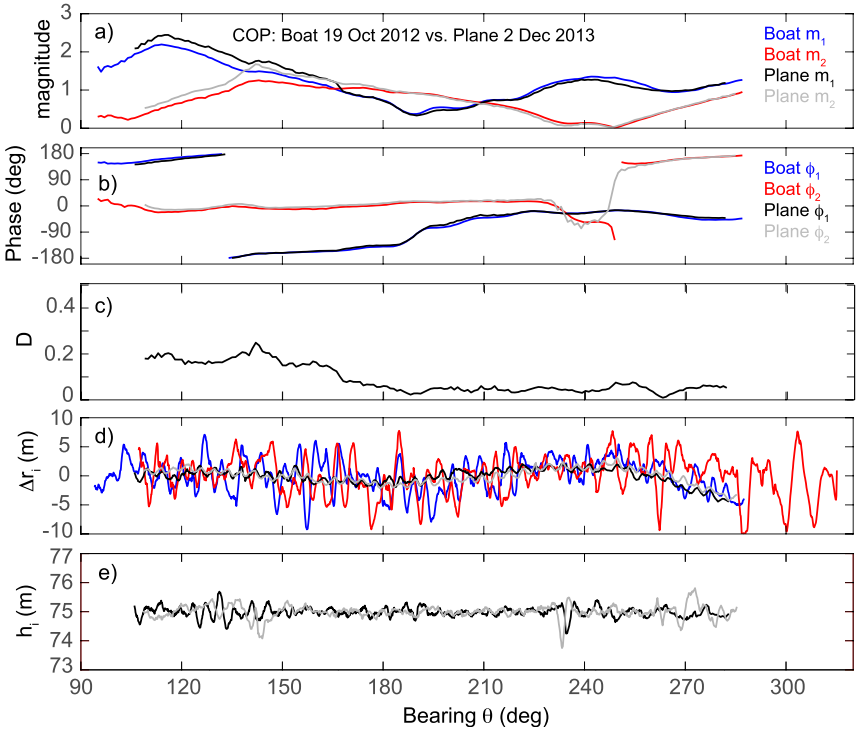

FIG. 2. (a) Magnitudes m_1 (black) and m_2 (gray) of loops 1 and 2, respectively, for antenna patterns obtained with a plane at COP. Magnitudes m_1 (blue) and m_2 (red) of loops 1 and 2, respectively, for antenna patterns obtained with a boat at COP. Dates of the patterns are indicated in the panel. (b) Phases ϕ_1 (black) and ϕ_2 (gray) of loops 1 and 2, respectively, for antenna patterns obtained with a plane at COP. Phases ϕ_1 (blue) and ϕ_2 (red) of loops 1 and 2, respectively, for antenna patterns obtained with a boat at COP. (c) Distance parameter D computed from the magnitudes and phases of (a) and (b), comparing the similarity of the APMs produced by the boat and plane. (d) Deviations from circular arcs Δr_i along two measurement paths traversed by the plane (black, gray) and by the boat Δr_i (blue, red). (e) Altitude h_i of the plane along two measurement paths traversed by the plane.

to incorporate into the smaller quadrotor. The dipole antenna had two elements, each 2.1 m long, constructed from 18-gauge wire. The electronics board was enclosed in a lightweight 3D-printed housing with the two dipole antenna elements extending from connectors on the ends of the housing. The mass of the signal source for the quadrotor, including the battery, was 0.076 kg. The electronics package, including the 12.6-V lithium polymer battery, was mounted between the antenna elements and the entire assembly was suspended below the quadrotor drone from the end of one of the antenna elements.

3. Results

a. Antenna pattern measurements from drones and boats

In this section we present representative examples comparing APMs among boats, planes, and quadrotors at three HF radar sites in the Southern California Bight: Coal Oil Point (COP), Nicholas Canyon (NIC), and Port San Luis (LUIS; Fig. 1). Once we determined that the drones could accurately reproduce the boat patterns, we discontinued using boats for APMs due to cost. Between January 1998 and June 2016, we have produced 105 APMs at various HF radar sites on the coast of central and Southern California. Of these, 32 have been APMs with drones and these were conducted since the first drone APM on 12 November 2013.

In most boat–drone comparisons, APMs were made more than a year apart, but despite the time differences, the drone APMs were generally similar to the boat APMs, suggesting that many patterns were fairly stable over time. Figure 2 shows APMs at COP from a boat and a plane obtained 14 months apart. Amplitudes (Fig. 2a) and phases (Fig. 2b) versus bearing were similar for loop elements 1 and 2 of the receive antenna (loops 1 and 2, respectively). Amplitudes and phases of loops 1 and 2 in Fig. 2 have been normalized by the amplitudes and phases of receive antenna element 3 (monopole) as discussed below. Near superposition at many bearings

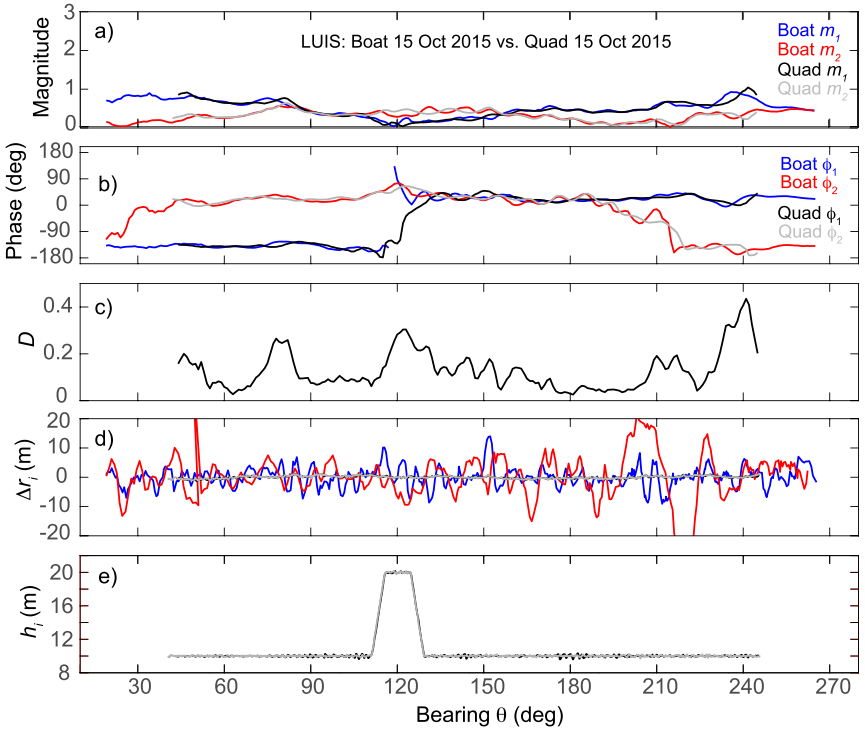

FIG. 3. (a),(b) As in Figs. 2a and 2b, respectively, but for quadrotor and boat at LUIS, both on 15 Oct 2015. (c) As in Fig. 2c, but for LUIS. (d) As in Fig. 2d, but for quadrotor and boat at LUIS. (e) As in Fig. 2e, but for quadrotor at LUIS.

and similar amplitude and phase patterns for both loops indicated good agreement over much of the range of bearings. Differences in amplitude for loops 1 and 2 occurred between 105° and 170° (Fig. 2a), and differences in phase occurred for loop 2 around 250° (Fig. 2b).

APMs were performed at LUIS with both a boat and a quadcopter on the same day (15 October 2015) and also showed good agreement in amplitude and phase for both loops over most of the bearing range (Fig. 3). Exceptions occurred around 120°, where the quadrotor altitude was increased from 10 to 20 m due to crossing a jetty (Fig. 3e) and around 240° near the end of the pattern. Amplitude differences for loop 2 occurred near the jetty and for loop 1 from 230° to 250°. The location of the jetty coincided with a phase difference of loop 1 exceeding 100° (Fig. 3b). We speculate that these amplitude and phase differences as the quadrotor rose over the jetty resulted from multipath effects of the jetty itself or from more of the direct signal, versus the ground-wave signal, reaching the receive antenna. The quadrotor pattern was restricted to a smaller range of bearings due to the presence of people in the water near shore and on the beach.

Amplitudes and phases from a quadrotor and a plane at NIC compared well from APMs obtained about 18 months apart (Fig. 4). Amplitude differences were larger for loop 2 than for loop 1, especially over bearings from 95° to 205° (Fig. 4a). Phase differences were small for both loops except for loop 2 around 260° and loop 1 near 150° (Fig. 4b).

b. *Quantification of APM differences*

To quantify the differences in APMs among boats, planes, and quadrotors, we used the APM difference parameter D following Emery et al. (2014). Parameter $D(\theta)$ is the magnitude of the difference (i.e., the Euclidean distance) between the complex antenna pattern vectors at each bearing θ from two APM methods. In computing $D(\theta)$, the complex vector for each APM method representing the responses of the two loops $\mathbf{a}'_k(\theta)$, where $k = 1, 2$, is normalized by the response of the monopole $\mathbf{a}'_3(\theta)$. The resulting normalized response vectors are

$$\begin{aligned}\mathbf{a}_k(\theta) &= \mathbf{a}'_k(\theta)/\mathbf{a}'_3(\theta) = [m_k(\theta)'/m'_3(\theta)]\exp[\phi'_k(\theta) - \phi'_3(\theta)]\\ &= m_k(\theta)\exp[\phi(\theta)_k],\end{aligned} \tag{1}$$

where the Euler relation has been used, m are the vector magnitudes, and ϕ are the phases of $\mathbf{a}'_k$ and $\mathbf{a}_k$. Magnitudes $m_k(\theta)$ of $\mathbf{a}_k$ are shown in Figs. 2a, 3a, and 4a and corresponding phases $\phi(\theta)_k$ are shown in Figs. 2b, 3b, and 4b, respectively. The real (Re) and imaginary (Im)

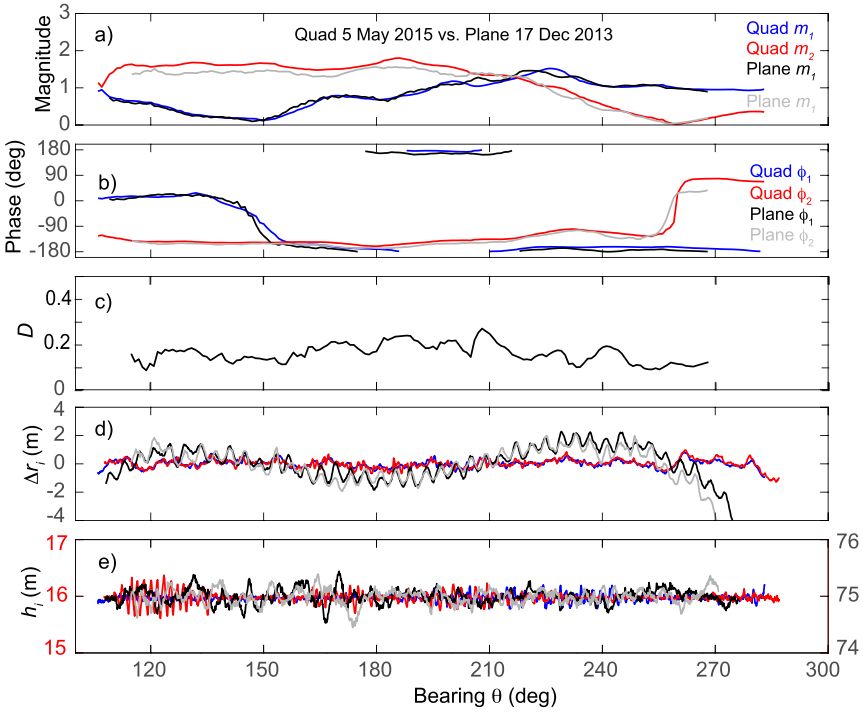

FIG. 4. (a),(b) As in Figs. 2a and 2b, respectively, but for quadrotor and plane at NIC. (c) As in Fig. 2c, but for NIC. (d),(e) As in Figs. 3d and 3e, respectively, but for quadrotor and plane at NIC.

parts of $\mathbf{a}_1(\theta)$ and $\mathbf{a}_2(\theta)$ are then combined into a column vector,

$$\mathrm{A}(\theta) = \{\mathrm{Re}[\mathbf{a}_1(\theta)]\,\mathrm{Im}[\mathbf{a}_1(\theta)]\,\mathrm{Re}[\mathbf{a}_2(\theta)]\,\mathrm{Im}[\mathbf{a}_2(\theta)]\}^{\mathrm{T}}, \quad (2)$$

where superscript T means transpose. Differences in APMs between methods—say, between a boat ($\mathbf{A}_B$) and a quadrotor ($\mathbf{A}_Q$)—are then given by

$$D(\theta) = \{[\mathbf{A}_B(\theta) - \mathbf{A}_Q(\theta)]^{\mathrm{T}}[\mathbf{A}_B(\theta) - \mathbf{A}_Q(\theta)]\}^{1/2}. \quad (3)$$

Values of D in Figs. 2c, 3c, and 4c are typical of the APM comparisons we made. For example, at COP, D declined from ~0.2 to less than 0.1 for θ between 109° and 167° (Fig. 2c), corresponding to decreasing differences in m_1 and m_2 (Fig. 2a). At LUIS, D exceeded 0.2 as altitude changed from 10 to 20 m over the jetty for θ between 118° and 132°, between 76° and 83°, and near the end of the pattern for $\theta > 232°$ (Fig. 3c). Differences in both m_1, m_2 and ϕ_1, ϕ_2 contributed to the D values exceeding 0.2 for these bearings (Figs. 2a and 2b). We speculate that multipath reflections from the jetty, or from a nearby pier, or both, accounted for $D > 0.2$ at LUIS. At NIC, D exceeded 0.2 between 181° and 213° due to differences in m_1, m_2; differences in ϕ_1, ϕ_2 were small over this range of θ. For comparison, Emery et al. (2014) found D ranging between 0.1 and 0.4 for boat APMs obtained as much as 4 years apart.

c. *Trajectories for antenna pattern measurements*

APM processing software requires small radial velocities to minimize Doppler frequency shifts in the received signals. By flying circular measurement paths centered on the receive antenna locations, low radial velocities were obtained, with consequent small Doppler frequency shifts. This procedure enables the processing software to track the signal source and increases the signal-to-noise ratio (SNR) by concentrating the calibration signal in a narrow range of frequency bins. It is assumed that the accuracy of the APM is related to the SNR (cf. Emery et al. 2014).

The boat, quadrotor, and plane were able to follow circular paths very closely, such as for APMs at COP (Fig. 5). In traversing the paths, the quadrotor and plane were under robotic control and the boat was under human control guided by shipboard GPS. To quantify the accuracy of the APM paths, circular arcs were fitted to the paths by using the radii and centers of the arcs (latitude and longitude) as free parameters. For all three platforms, the fitted arcs and the paths were indistinguishable when graphed at the scale in Fig. 5. Deviations of the measured paths compared

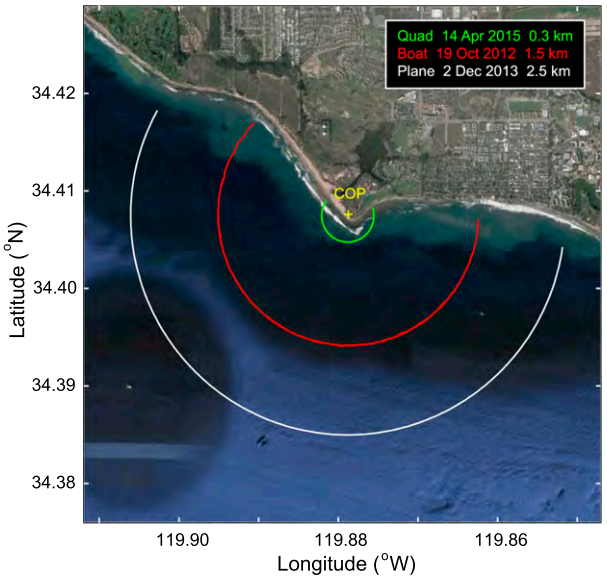

FIG. 5. Paths followed by quadrotor, boat, and plane during APMs at COP. Legend gives platform, APM dates, and radii of circular measurement paths. The plane and boat paths correspond to the APMs of Fig. 2. The quadrotor path is from an APM at COP (data not shown). Underlying image is from Google Earth.

with the fitted arcs however differed substantially among the platforms.

The difference in radial distance Δr_i at each location i between the path and the fitted arc was interpreted as a measure of path accuracy. Term Δr_i was estimated at each bearing θ_i, where a platform obtained a GPS fix as

$$\Delta r_i = r(\theta_i) - r_f, \tag{4}$$

where r_f is the radius of the fitted circle. The centers of the fitted circles were typically within a few meters of the receive antenna locations. For the boats Δr_i was often within ±10 m but occasionally exceeded ±15 m (Figs. 2d, 3d, and 4d). In contrast, for the quadrotors Δr_i was typically within ±1 m and often within ±0.5 m (Figs. 3d and 4d). For the planes Δr_i was intermediate, typically within ±2 m, although low-frequency excursions were occasionally larger (Figs. 2d and 4d). The planes also exhibited sinusoidal variations in Δr_i possibly due to ''underdamping'' by the control systems as they attempted to maintain circular arcs (Figs. 2 and 4).

To quantify the overall differences between the measurement paths and circular arcs, root-mean-square (rms) differences $\Delta r_{\rm rms}$ were calculated as

$$\Delta r_{\rm rms} = \left(\frac{1}{N}\sum_i \Delta r_i^2\right)^{1/2}, \tag{5}$$

where N is the number APM locations. The $\Delta r_{\rm rms}$ values were measured for the two traverses of the arcs during the APMs of Figs. 2–4. Values of $\Delta r_{\rm rms}$ for APMs of Figs. 2–4 were less than 1 m for the quadrotors, 1–2 m for the planes, and 3–9 m for boats.

Radial velocities produced by the boats, quadrotors, and planes were computed with centered first differences as

$$v_{ri} = (\Delta r_{i+1} - \Delta r_{i-1})/2\Delta t, \tag{6}$$

where subscript i indicates location, Δr_i is from (4), and Δt is the time interval between measurements of r_i. For the planes and quadrotors Δt was ~0.5 s and for the boat Δt was ~10 s. For all three platforms during transects along the APM measurement arcs, values of v_r were less than 1 m s^{-1}. Values of v_r from typical arcs are shown in Fig. 6. The boat had the greatest range in v_r (Fig. 6a) followed by the plane (Fig. 6c) and quadrotor (Fig. 6b). Standard deviations for v_r shown in Fig. 6 were 0.18, 0.08, and 0.19 m s^{-1} for the boat, quadrotor, and plane, respectively. The slower flight speed and smaller Δr_i combine to produce the lower v_r for the quadrotor, which is an advantage for APMs, since distortions caused by radial platform speeds are smaller.

The quadrotors and planes using onboard atmospheric pressure measurements were typically able to control their altitudes within ±1 m of the programmed altitude of the APM (Figs. 2e, 3e, and 4e). During the quadrotor APM at LUIS, for example, altitude was maintained at 10 ± 0.5 m except for the excursion to 20 m to avoid the jetty (Fig. 3e). At NIC the quadrotor altitude was 16 ± 0.4 m with sinusoidal oscillations from 110° to 130° (Fig. 4e). Altitude was computed relative to the launch elevation, and at NIC the quadrotor launch elevation was about 12 m above sea level, so the altitude above water ranged from about 15 to 17 m as shown in Fig. 4e. The plane for the NIC APM was launched near sea level. For the APMs at LUIS and COP, the quadrotor launch elevations were also near sea level. The rms differences in altitude $\Delta h_{\rm rms}$ were computed as

$$\Delta h_{\rm rms} = \left[\frac{1}{N}\sum_i (h_i - \overline{h})^2\right]^{1/2}, \tag{7}$$

where h_i is altitude at location i and $\overline{h}$ is the mean altitude. For the quadrotors and planes, $\Delta h_{\rm rms}$ ranged from 0.1 to 0.2 m for the APMs at COP, LUIS, and NIC.

4. Summary

We employed small aerial drones to conduct APMs of oceanographic HF radars for observing ocean surface currents. Figure 7 shows an example of a quadrotor

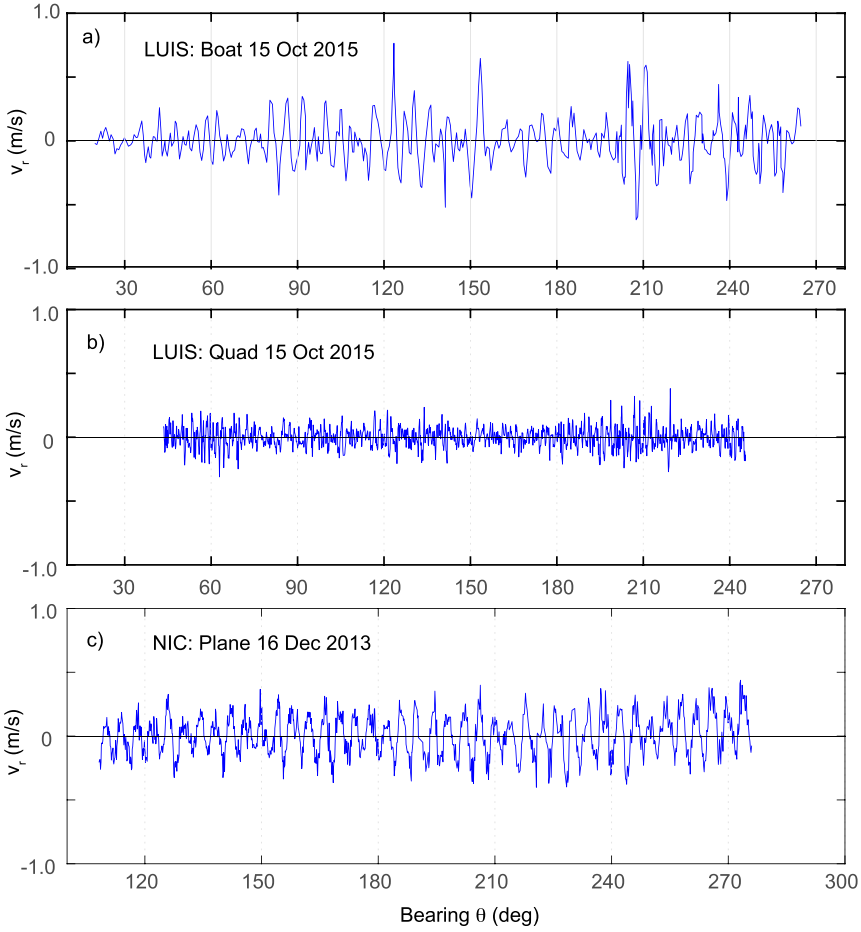

FIG. 6. Radial velocity v_{ri} during APMs from (a) boat at LUIS, (b) quadrotor at LUIS, and (c) plane at NIC. APM dates are shown in the panels.

drone carrying a signal source in flight at the beginning of an APM. The approach using aerial drones has several advantages compared with the conventional ship-based approach. First, costs are lower, since research vessels are not used and fewer personnel are required. Second, patterns are more easily obtained at remote sites that may be difficult to access with small research vessels. Third, the ability to measure patterns is not as strongly dependent on environmental conditions. For example, sea state is less of a factor than with ship-based patterns, although high winds limit both approaches. Fourth, although not demonstrated here, drones can measure patterns closer to shore, since they are not affected by the surfzone and other hazards associated with vessels being close to shore.

Comparisons here demonstrate a high degree of similarity between APMs obtained with the boat-based method and drone methods. Given this similarity, we conclude that relevant radio wave propagation characteristics in boat-based APMs, such as ground wave propagation, are reproduced in drone-based patterns. Reasons for observed differences in the APMs between platforms are uncertain, but in some cases may result from changes in the local environment over the 1-yr or longer time differences for several APM comparisons. Multipath effects may also contribute, for example, due to differences in signal propagation between measurement paths of 300 m versus 2500 m from the radars of the quadrotors and planes, respectively. Lower radial velocities of the quadrotors are an advantage since they result in fewer points in APMs being rejected due to excessive radial velocity.

Preliminary results suggest APMs depend on altitude and future APM experiments will explore this sensitivity. We speculate that if the altitude of the APM path is a large fraction of the range to the radar (i.e., the elevation angle above the receive antenna is large), then APM differences result from differences between measuring the pattern of the ground wave propagation versus measuring the pattern of the direct signal. More experimentation is required, but the results here indicate that

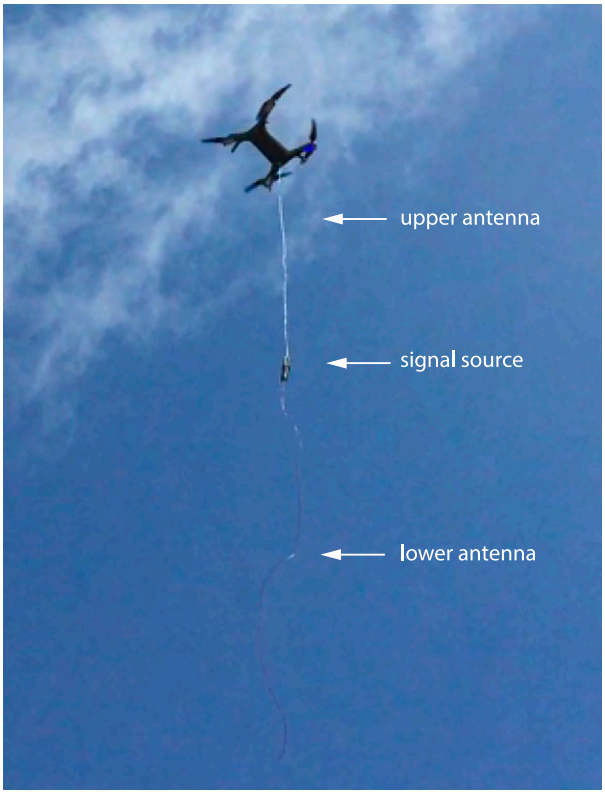

FIG. 7. Quadrotor in flight during an APM with a dipole signal source suspended below.

the 300-m ranges and 10–20-m altitudes of the quadrotors, and the 2500-m ranges and 75-m altitudes of the planes, produce satisfactory APMs.

The use of aerial drones is rapidly expanding worldwide and regulations governing their use for a wide range of applications, including scientific research, are currently being developed. These regulations may limit some operations using aerial drones for APMs. For example, our use of planes flying 2.5-km arcs around radar sites for APMs is no longer permissible (as of June 2016) because the planes were beyond visual range of the unaided eye during much of their flight trajectories. Regulations developed by the U.S. Federal Aviation Administration in 2016 included the need for ''see and avoid'' capabilities, requiring visual contact with drones at all times. Therefore, this requirement expressly prohibits this mode of operation. However, so-called first-person viewing technologies in which a human operator can obtain real-time high-definition video from drones may result in modification of this restriction in the future.

The ability to measure APMs accurately and quickly with aerial drones is useful in establishing temporary oceanographic radar installations in response to environmental incidents, such as oil spills. For example, in May 2015 we deployed and operated a solar-powered HF radar site to assist in tracking an oil spill at Refugio State Beach, California. Within several hours of establishing the site at Gaviota, California, near the spill, one of us (author ER) measured the antenna pattern for the site using a quadrotor. The measured pattern was soon thereafter incorporated into the real-time processing of radials and total surface vectors for display on the website of the Southern California Coastal Ocean Observing System (www.sccoos.org). Data from the Gaviota site with measured antenna patterns improved coverage of surface current vectors near shore.

Drone technologies are developing rapidly and we expect their capabilities for APMs to increase correspondingly. Improvements in automated flight control and navigation seem likely to increase the overall reliability of drones and to improve their ability to fly precise trajectories in a broader range of weather conditions. The ability of drones to robotically take off, fly precise trajectories for APMs, and then land at their takeoff sites will simplify the conduct of APMs. Increases in energy storage of batteries will lengthen flight durations. This in turn will allow drones to conduct APMs over broader arcs within coverage areas of oceanographic radars. Multirotor drones are now available in off-the-shelf configurations that have the programming capability and battery duration, such that they can be routinely used by HF radar operators for APMs. This in turn will improve the data quality of evolving large-scale oceanographic radar networks.

Acknowledgments. The authors thank David Salazar and Ian Robbins for their work in conducting antenna patterns from small boats and in maintaining the HF radar network. The authors also thank undergraduate students Lance Lowenberg, Erinn Sloan, and Brandon Gundberg of the Department of Mechanical Engineering at the University of California, Santa Barbara, for their assistance in constructing and testing the drones. Project funding was provided by the NOAA Integrated Ocean Observing System (448750-22571 to LW) through the Southern California Coastal Ocean Observing System. One of the authors (LW) also donated funding for the project. Additional funding was provided by the National Science Foundation Grant OCE-1031893 and Grant OCE-1232779 to the Santa Barbara Coastal Long Term Ecological Research (SBC LTER) project.

REFERENCES

Barrick, D. E., and B. J. Lipa, 1999: Using antenna patterns to improve the quality of SeaSonde HF radar surface current maps. *Proceedings of the IEEE Sixth Working Conference on*

Current Measurement, S. P. Anderson et al., Eds., IEEE, 5–8, doi:10.1109/CCM.1999.755204.

Cosoli, S., A. Mazzoldi, and M. Gačić, 2010: Validation of surface current measurements in the northern Adriatic Sea from high-frequency radars. *J. Atmos. Oceanic Technol.*, **27**, 908–919, doi:10.1175/2009JTECHO680.1.

de Paolo, T., and E. Terrill, 2007: Skill assessment of resolving ocean surface current structure using compact-antenna-style HF radar and the MUSIC direction-finding algorithm. *J. Atmos. Oceanic Technol.*, **24**, 1277–1300, doi:10.1175/JTECH2040.1.

Emery, B. M., L. Washburn, C. Whelan, D. Barrick, and J. Harlan, 2014: Measuring antenna patterns for ocean surface current HF radars with ships of opportunity. *J. Atmos. Oceanic Technol.*, **31**, 1564–1582, doi:10.1175/JTECH-D-13-00181.1.

Fernandez, D. M., J. F. Vesecky, and C. C. Teague, 2003: Calibration of HF radar systems with ships of opportunity. *Proceedings of the 2003 IEEE International Geoscience and Remote Sensing Symposium*, Vol. 7, IEEE, 4271–4273, doi:10.1109/IGARSS.2003.1295486.

——, ——, and C. Teague, 2006: Phase corrections of small-loop HF radar system receive arrays with ships of opportunity. *IEEE J. Oceanic Eng.*, **31**, 919–921, doi:10.1109/JOE.2006.886238.

Flores-Vidal, X., P. Flament, R. Durazo, C. Chavanne, and K. W. Gurgel, 2013: High-frequency radars: Beamforming calibrations using ships as reflectors. *J. Atmos. Oceanic Technol.*, **30**, 638–648, doi:10.1175/JTECH-D-12-00105.1.

Kissack, B., 2012: Exploration of a low-cost autopilot system for use in academe. M.S. thesis, Dept. of Aerospace Engineering, Wichita State University, 78 pp. [Available online at http://soar.wichita.edu:8080/handle/10057/5531.]

Kohut, J. T., and S. M. Glenn, 2003: Improving HF radar surface current measurements with measured antenna beam patterns. *J. Atmos. Oceanic Technol.*, **20**, 1303–1316, doi:10.1175/1520-0426(2003)020<1303:IHRSCM>2.0.CO;2.

Lipa, B. J., and D. E. Barrick, 1983: Least-squares methods for the extraction of surface currents from CODAR crossed-loop data: Application at ARSLOE. *IEEE J. Oceanic Eng.*, **8**, 226–253, doi:10.1109/JOE.1983.1145578.

Paduan, J. D., K. C. Kim, M. S. Cook, and F. P. Chavez, 2006: Calibration and validation of direction-finding high-frequency radar ocean surface current observations. *IEEE J. Oceanic Eng.*, **31**, 862–875, doi:10.1109/JOE.2006.886195.

Schmidt, R. O., 1986: Multiple emitter location and signal parameter estimation. *IEEE Trans. Antennas Propag.*, **34**, 276–280, doi:10.1109/TAP.1986.1143830.